**CONFERENCE PRE-PRINT**

# OVERVIEW OF THE ASDEX UPGRADE RESULTS

T. PÜTTERICH for the ASDEX Upgrade Team[1]
Max-Planck-Institut für Plasmaphysik
D-85748 Garching, Germany
Email: thomas.puetterich@ipp.mpg.de

**Abstract**

After a 26-month vent ASDEX Upgrade (AUG) went back in operation with a newly designed upper divertor featuring in-vessel coils, a charcoal coated cryo-pump and flat W-coated tiles. The coils enable alternative divertor configurations (ADCs), which explored via parameter scans and an extensive set of measurements was obtained. Interpretation and comparison to SOLPS are ongoing. Prompted by the ITER wall change, dedicated experiments at the beginning of the campaign on non-boronized plasma startup were contrasted to that employing asymmetric and symmetric boronizations. While the non-boronized startup was challenging due to limited available heating power, the asymmetric boronization proved to be as beneficial as the symmetric one, which is in contrast to previous model calculations. This discrepancy is possibly explained by the assumed sticking coefficient (perfect sticking) of boron, which deviates from the measured one (range of $\approx 0.3$). In the startup phase also the impurity influxes at the outboard limiters were investigated. In the unboronized case low-Z impurities play a major role in cooling down the plasma edge to low enough temperatures such that W sputtering is negligible. In the boronized case, the boron layers are eroded within $1-2\,$s of limiter contact and then a considerable W source and content is observed. Corresponding SOLPS calculations show good agreement and hint towards W self-sputtering. Pedestal stability investigations have identified the importance of various pedestal regions. The quasi-continuous exhaust (QCE) regime is obtained when ballooning modes are active at the bottom of the pedestal and the global peeling-ballooning stability is high enough. Thus, at high enough shaping and high gas flux both can be achieved and QCE is a consequence. The closely related enhanced D-alpha (EDA) mode is not clearly distinguishable from QCE, e.g. the quasi-coherent mode characteristic for EDA also shows up in QCE. In both QCE and EDA the impurity transport is behaving benign as could be measured for Ne with a comprehensive CXRS measurements on $Ne^{8+}$ to $Ne^{10+}$ ions. The ballooning instability increases the diffusive component of pedestal impurity transport and thus counteracts the neoclassical convection of impurities. For high radiative fractions the regime of the X-point radiator (XPR) is accessible at AUG and the understanding of its access conditions and behaviour is further developed. Due to the localized radiative cooling at the X-point the XPR can be well diagnosed and thus controlled. Ultimately, it combines high radiative fractions ($\approx 95\%$) with complete detachment and acceptable dilution and confinement ($H_{98,(y,2)} \approx 0.95$). For negative triangularity shapes, further experiments at increased shaping resulted in strongly heated L-mode plasmas avoiding ELMs. For beam heating obvious power degradation was observed and only during nitrogen seeding an elevated confinement was found. Core plasma modelling connecting plasma and impurity transport was benchmarked at AUG and allowed to extrapolate all transport channels towards ITER, showing that in the plasma core of ITER turbulent transport will be even more important relatively to neoclassical transport than in today's devices. Integrated modelling connecting core to SOL investigated the size scaling of confinement and arrived at a more optimistic outlook to ITER than the newest ITPA20-IL scaling suggesting a fusion yield of Q=12 for the baseline scenario. Further, investigations of the ITER ramp-down in AUG provide insights into maintaining position control. Various aspects of shattered pellet injection were investigated in AUG and one of the results show that with increasing Ne fraction the radiation during the current quench increases and the current decay becomes faster.

## 1. INTRODUCTION

The ASDEX Upgrade (AUG) programme is dedicated to addressing key physics challenges for ITER operation and to developing plasma scenarios for the future fusion devices. The AUG plasma ($R_0 = 1.65\,$m, $a = 0.5\,$m, $I_p \leq 1.4\,$MA, $B_t \leq 3.5\,$T) can be heated with up to $20\,$MW of neutral beam injection (NBI), $6\,$MW of electron cyclotron resonance heating (ECRH), and $5\,$MW of ion cyclotron resonance heating (ICRH), enabling a broad spectrum of plasma scenarios. Since 2007, the AUG first wall has been fully clad with tungsten (W), and the

[1] see ZOHM, H., et al, Nucl. Fusion 64 (2024) 112001, https://doi.org/10.1088/1741-4326/ad249d

operational experience accumulated since then is proving highly valuable for supporting the ITER re-baselining including the full-W wall. An extensive set of diagnostics provides detailed measurements, while plasma control is managed through the Discharge Control System (DCS), which is continuously advanced to expand the scope of real-time plasma regulation. The latter is also important for testing operational strategies of ITER already in ASDEX Upgrade.

During the long vent spanning from August 2022 to October 2024, a major upgrade of the upper divertor (1) has been performed, during which in-vessel coils (1; 2; 3), an additional cryo-pump (4) with charcoal and a reshaping of the first wall was performed providing access to a considerable variety of alternative divertor configurations (5) (cf. to Fig. 1). Hence, a major part of the programme was dedicated to exploiting these new capabilities and to perform a lay of the land concerning the accessibility and performance of the new configurations. Additional focus was put on the effect of uniformity of boronizations, W-erosion during limiter phases, transport and confinement of core and edge plasmas with a particular focus on ELM-free or small ELM scenarios. Further topic of interests are disruptions and their temporal tayloring employing the shattered pellet injection (SPI) system designed and installed in the course of an ITER collaboration.

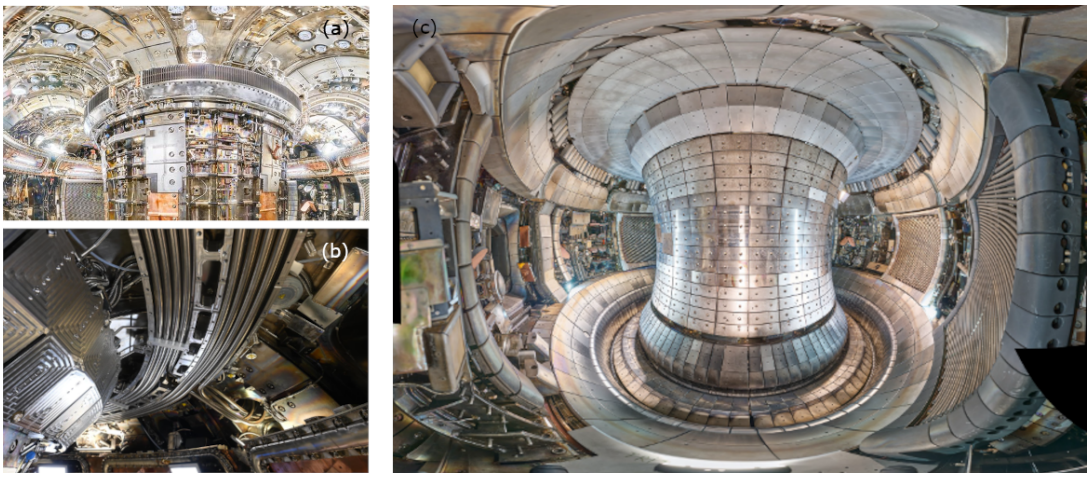


*FIG. 1. Invessel photographs during vent: (a) cryo-pump; (b) in-vessel coils after in-vessel bending and mounting; (c) view after mounting of all PFCs.*

## 2. STARTUP WITH NO, SYMMETRIC AND ASYMMETRIC BORONIZATION

After the long vent ASDEX Upgrade underwent the standard procedure of baking and leak searches (6) and the first discharges were attempted without boronization (7). Unlike the unboronized restart in 2008 (8; 9), neutral beam injection was not yet available for restart, while ECRH was available. However, due to the less developed ECRH interlock procedures less power was used during the restart, which led to a slower conditioning progress. Consequently, the burn-through at the plasma ramp-up was deteriorated leading to long phases with increased loop voltages and the creation of run-away beams (10; 11). This is documented in Fig. 2, in which the upper row shows the plasma before the first boronization using ECRH during current ramp-up, but then failing the maintenance of the current due to excessive radiation from low-Z elements. The lower row in Fig. 2 corresponds to the first plasma

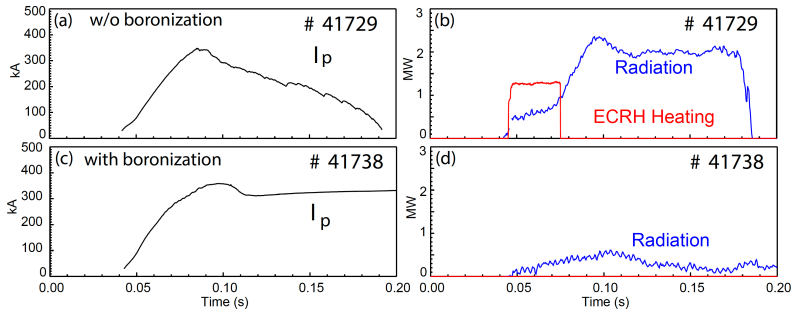


*FIG. 2. (a),(b) Trajectories of plasma current, ECRH, Ohmic heating and radiated power at the end of the unboronized restart. (c),(d) Same for the first discharge after boronization.*

discharge after boronization, in which ECRH was not necessary. After the occurrence of large runaway electron contributions to the plasma current the decision to boronize before fully establishing plasma operation was made. This first boronization was performed via a glow discharge using only two (sector 3 and 8) out of four anodes (sectors 3, 8, 14 and 16), however, the subsequent plasma startup worked with the first attempt documenting the strong benefit even from an asymmetric boronization. Subsequent boronizations were then used to quantitatively compare symmetric (sec. 3, 8, 14 and 16) to asymmetric boronizations (without 8) and as can be seen in Fig. 3, a considerable amount of boron is deposited in sector 8 even though the anode was not active (10). The measured

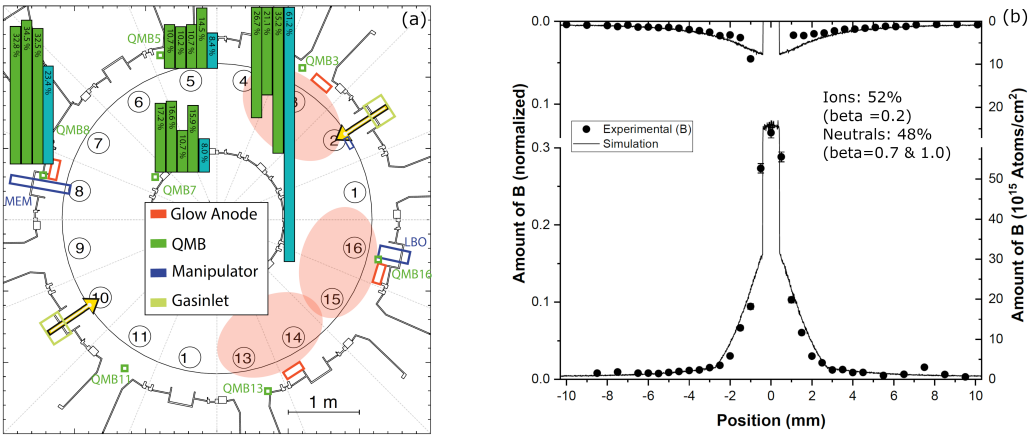


*FIG. 3. (a) Overview of important actuators and measurements for performing and characterizing each boronization (adapted from (10)). Bars indicate the extrapolated deposited boron amount using the various quartz micro balance locations as a fraction of the boron gas influx. Light green give the percentage for symmetric boronizations using (anodes in sectors 3, 8, 14 and 16) and turquoise corresponds to one asymmetric boronization (3, 14, 16). (b) Analysis of a cavity probe for evaluating the sticking coefficient of boron molecules (12). Beta is the surface loss probability showing very small sticking for neutrals.*

amounts in sector 8 are much larger than the ones expected from modelling (model cf. to (13)) and this is probably related to the boron molecule sticking coefficient being assumed 1 in the model, while in experiment cavity probes revealed it to be in the range of $\approx 0.3$, which is a weighted mix of ion and neutral sticking. This suggests that the boronization result is more symmetric than originally believed even if fewer anodes are available, which could give more freedom in the anode positioning in ITER.

## 3. W-EROSION DURING THE LIMITER PHASE

Due to the re-baselining of ITER (14), the erosion of W and the underlying mechanisms have moved into focus (e.g. (15)). One of the important aspects in ITER is the behaviour of boron layers and W erosion during the limiter phase and its impact on the core plasma and correlated effects on the current ramp-up (16). In order to address these topics, experiments in AUG were performed studying limiter discharges before and after the first boronization. Before the first boronization strong radiation from low-Z elements cooled down the plasma edge of limited discharges such that W erosion was not detectable. For the first discharges #41876 and #41877 after boronization, a rapid erosion of boron is observed. This becomes visible, when examining Fig. 4. In the first phase ($t < 2.4$ s) of #41876 B is strongly eroded (Fig. 4(b)) and no W-influx (Fig. 4(c)) is observed. After $t = 2.4$ s W-erosion is observed. As the heating power is also increased at 2.4 s from 0.6 MW to 1.3 MW, it is instructive to compare to the subsequent discharge (Fig. 4(d) and (e)) with the same heating sequence. W-erosion is observed from the beginning at a stable level, demonstrating that the erosion areas of the limiters are already free of protecting B. These and further measurements allow for benchmarking the models which may then be used to investigate the limiter phases in ITER.

## 4. ADVANCED DIVERTOR CONFIGURATIONS

After the major upgrade of the upper divertor the alignment quality from tile to tile was checked by comparing L-mode discharges with flipped B-field directions. A good symmetry between both cases and from tile to tile was observed and throughout the campaign this good alignment did not deteriorate. Subsequently, the alternative divertor configurations were created and studied in AUG (17). In Fig. 5 six prominent configurations are depicted including the non-ADC single null configuration (SN). The X-divertor (XD) features an increased flux expansion

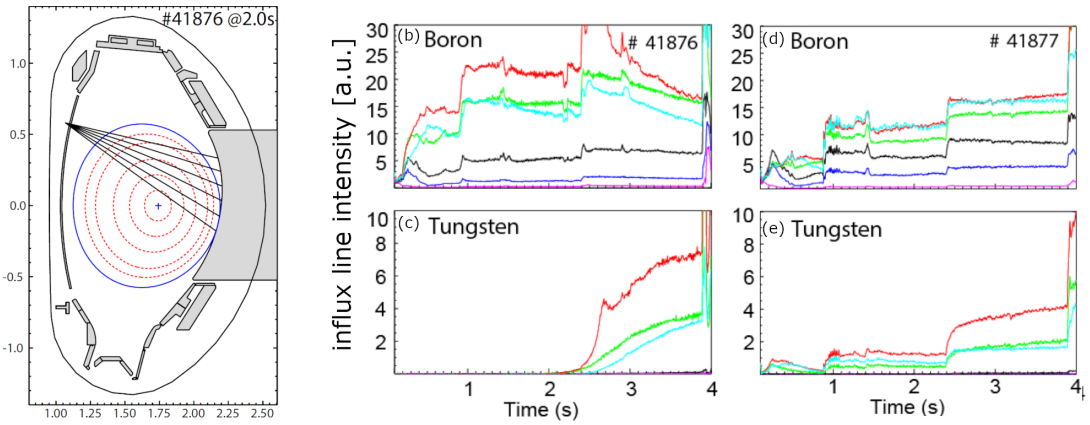


*FIG. 4. (a) Plasma equilibrium and lines of sight (LOS) of the limiter erosion measurement (b) Photon fluxes of $B^{1+}$ on the LOS depicted in (a) from #41876, higher fluxes are measured by lower LOSs. (c) Photon flux of $W^0$ from #41876. (d) Same as a (b) but from #41877. (e) Same as (c) but from #41877*

at the strike-point (SP), while the super compact radiative divertor (sCRD) is characterized by an increased flux expansion at the X-point and a closeness of the X-point to the first wall. The various snowflake configurations

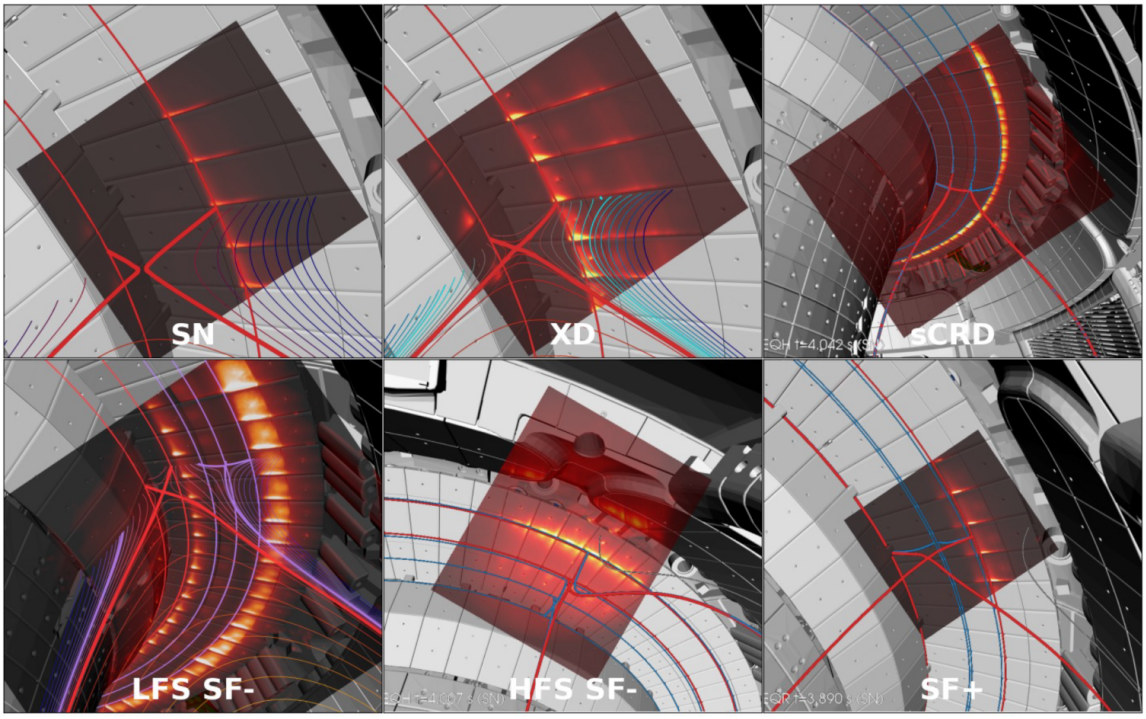


*FIG. 5. ADC configurations as reconstructed from a equilibrium reconstruction together with infrared measurements in the CAD visualized interior of AUG. The created configurations are single null (SN) for reference, X-divertor (XD), super compact radiative divertor (sCRD), LFS snowflake minus (LFS SF-), HFS snowflake minus (HFS SF-) and snowflake plus (LFS SF-)*

feature a second X-point either on the high-field side scrape-off layer (HFS SF-), low-field side scrape-off layer (LFS SF-) or in the private flux region (SF+) of the primary X-point. The power foot print, as measured by an infrared (IR) camera, for all cases clearly show that the alternative configurations are not only seen in the reconstructed equilibria, but are also altering the power footprints at the strike lines. In Fig. 6, the power footprints, for SN, XD and LFS SF- configurations are depicted in more detail. In particular, a pronounced second power peak is appearing for the ADCs at the secondary SP for the LFS SF- configuration. This peak is of high interest as its magnitude is comparable to that of the primary SP. Important parameters for detachment might influence the power to the primary SP first, while the power splitting between both SP is closely related to the upstream power fall off length. It should be noted that the IR measurements are ELM averaged and more work is needed

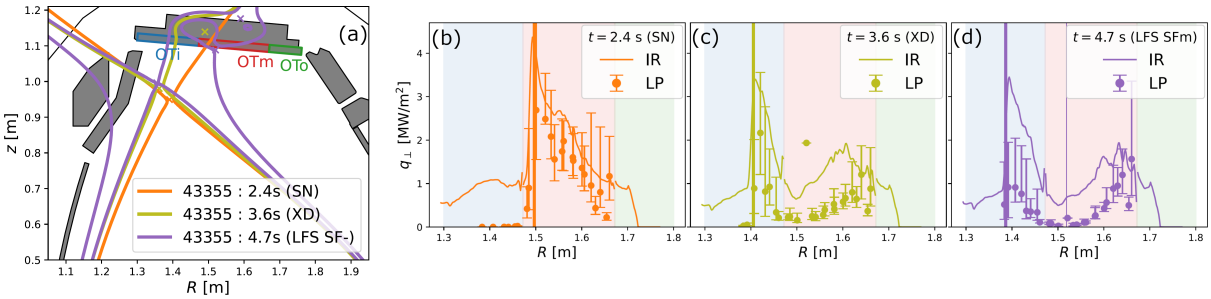


*FIG. 6. (a) Separatrix geometry for three divertor configurations. (b) Power footprint derived from an IR camera and Langmuir probes for the SN configuration.(c) Same for XD (d) Same for the LFS SF-.*

to ultimately compare the result to modelling. In order to collect a comprehensive set of data for restraining models a large diagnostic suite was implemented in parallel with the upgrade of the upper divertor. In Fig. 7, the geometry of several main diagnostics is depicted. The SP are diagnosed with high resolution and the divertor

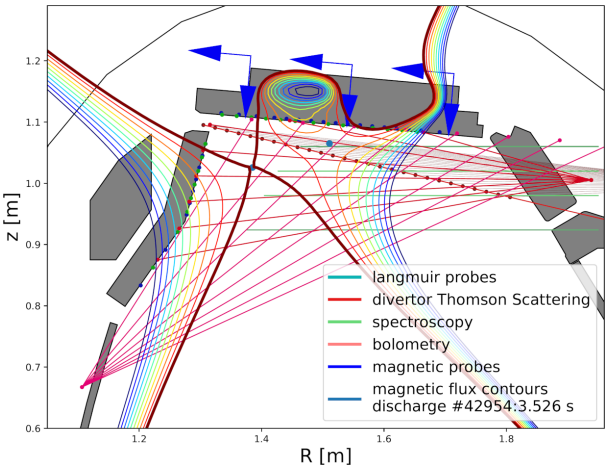


*FIG. 7. Geometry of some main diagnostics in the upper divertor implemented for a comprehensive evaluation of the divertor performance and for restraining model calculations such as SOLPS. The equilibrium reconstruction corresponds to a LFS SF- configuration.*

volume is monitored with Thomson scattering and many LOS from bolometry and spectroscopy. The magnetic probes restrain the equilibrium reconstruction. In Fig. 8, example measurements of additional spectroscopy LOS are depicted. The LOS are visible in the left top panel of Fig. 8, and on the right a full sequence of the reconstructed parameters of the spectroscopic measurements is depicted. The marked time points 2.8 s 3.5 s and 3.9 s correspond to the reconstructed equilibria on the left. Even though the intensity of $D_\epsilon$, the electron density and the intensity of a $N^{+1}$ line are LOS integrated a clear movement of the emission and density fronts is visible. Deconvoluting this data and combining it with the measurements from other diagnostics will give good guidance to restraining model runs such as from SOLPS.

Generally, large parameter scans in heating (up to 20 MW), fueling and seeding (N, Ne, Ar and Kr) were performed, while the inner SP was constantly detached. There were clear signs that the divertor compression suffers from the open divertor geometry and thus better performance is expected for a future implementation of divertor baffels. As a next step the performance of the ADCs will be compared and the best performing configuration will be the basis for planning the baffels. The latter will hinder the comprehensive diagnostics and thus will be implemented only after 2028.

## 5. CALMING THE PLASMA EDGE

Avoiding large type-I ELMs is an obligatory goal for future fusion devices and thus, investigations at AUG are pursued also in this direction. A major goal is achieving ELM-free or small ELM-phases instead, but at the same time impurity exhaust is also mandatory.

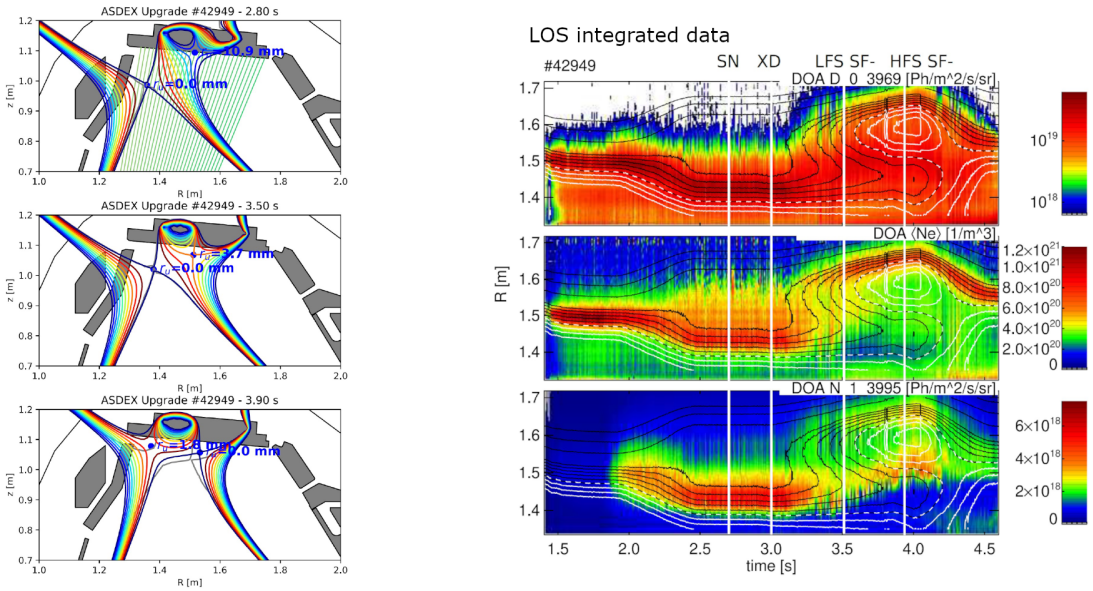


*FIG. 8. Left Column: The equilibrium reconstructions for XD, LFS SF- and HFS SF- are presented. In the top plot LOS from spectroscopy used in the left column are depicted. Right Column: A colour map depicts the radial dependence of the LOS integrated values for the $D_\epsilon$ intensity, the electron density derived from Stark broadening and the intensity from the $N^{+1}$ line at 399.5 nm.*

### 5.1. QCE/EDA

A very promising regime for obtaining tolerable heat and particle exhaust via small ELMs is the quasi-continuous exhaust (QCE) regime (recent AUG work (18)) which is often difficult to distinguish from the enhanced D-alpha (EDA) regime (recent work (19)), as features that are attributed to each regime are observed sometimes in coexistence. An example for this is the quasi-coherent mode (QCM) (20). As the QCE regime features also beneficial power fall-off length (21; 22; 23) it is considered an interesting reactor regime. As a first step it was also ported and investigated at JET, also in JET DT (24). A major breakthrough was obtained by analysing the stability of the pedestal in various radial regions (25; 26). The global pressure of the pedestal is one player responsible for the large type-I ELM crash, the local pressure at the foot of the pedestal may give rise to small scale ballooning instabilities, which are believed to be be characteristic for the QCE regime. In Fig. 9(a) (adapted from (27)), the normalized pressure gradient $\alpha$ from the equilibrium reconstruction (green), which is at the peeling-ballooning limit, is compared to the infinite-n ballooning limit (purple). At the plasma edge, this limit is almost achieved and

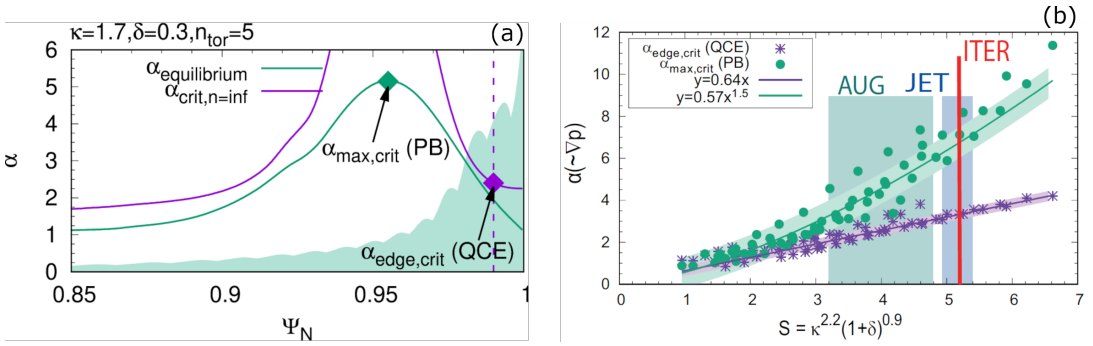


*FIG. 9. (a)The $\alpha$-profile (green) corresponding to a specific case in AUG is unstable to finite-n peeling-ballooning modes, and defines at its maximum $\alpha_{max,crit}$. The mode envelope for the $n = 5$ mode is shown as the shaded region. The purple $\alpha$ profile corresponds to the local onset of infinite-n modes at each radius defining $\alpha_{edge,crit}$ at an chosen radius at the edge (dashed, vertical line). (b) Critical $\alpha$s for global peeling ballooning modes (green) and local ballooning modes (purple) as a function of the shaping parameter S.*

an increase in the plasma shaping increases the limit for finite-n peeling-ballooning (here $\alpha_{max,crit}$ is used as a proxy) more pronounced than the infinite-n ballooning limit $\alpha_{edge,crit}$, which then leads to the pressure profile being limited by the infinite-n ballooning limit close to the separatrix. This latter state is suggested to apply for

the QCE regime (27). In Fig. 9 (b), the dependence of the two critical $\alpha$ values is visualized for several cases with different shaping, demonstrating that the elongation $\kappa$ and triangularity $\delta$ play a crucial role, which can be approximately summarized by $S$. At higher values of $S$ the headroom for $\alpha_{max,crit}$ grows and the plasma has easier access to the QCE regime. This is especially applying to shaped plasmas in JET and ITER, as their shaping accesses even higher values of $S$. As an encouraging observation QCE is also found (28) in GRILLIX (29) simulations, which then also could be used as a tool for extrapolation to other devices.

### 5.2. Impurity transport

An amelioration of ELMs at good confinement always yields the question for impurity exhaust. Especially at the transport barrier at the plasma edge potentially an excessive impurities confinement is possible. In Fig. 10, the result of a data analysis based on Bayesian inference (30) is presented. The analysis could separate the diffusive

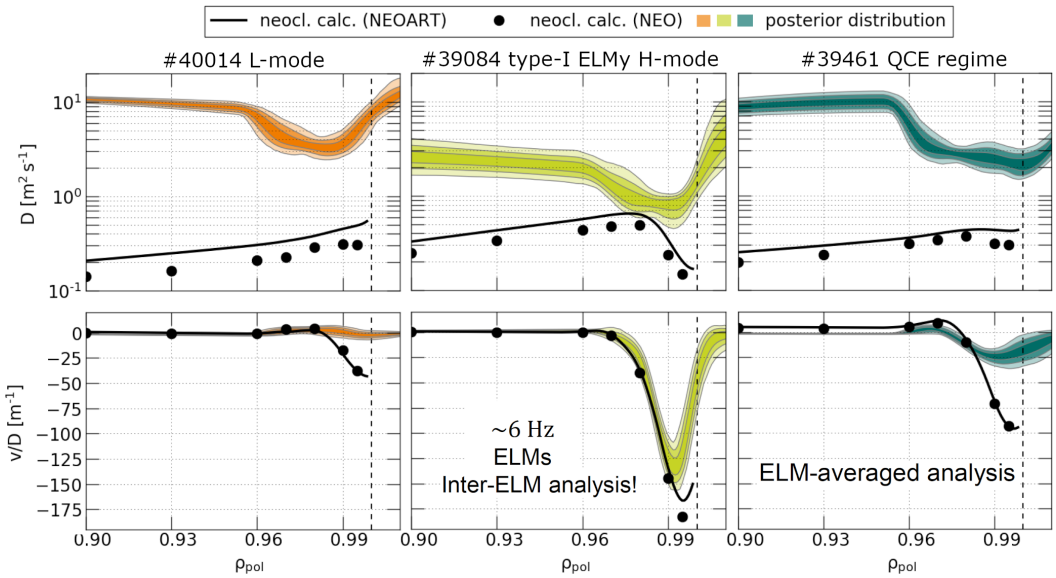


*FIG. 10. Left column: The diffusion coefficient D (top) as determined via Bayesian inference in colour is compared to neoclassical results for an L-mode discharge. The drift parameter v/D (bottom) is compared to the corresponding predictions for the same discharge. Middle column: Same but for the inter ELM-phase of a type-I ELMy H-mode discharge. Right column: Same but for an H-mode in the QCE regime. For QCE, the analysis is ELM averaged due to the high frequency of ELMs.*

and convective transport of Ne remarkably well, because the CXRS measurements from several Ne ions, i.e. $Ne^{8+}$, $Ne^{9+}$ and $Ne^{10+}$ are combined. The results are compared to neoclassical predictions. In the first column of Fig. 10 the results for L-mode show clearly that neoclassical transport is not sufficient to describing the observed Ne diffusivity and additional, i.e. turbulent transport is postulated. Thus, the v/D ratio, which is proportional to the normalized Ne-density gradient is small throughout the plasma edge. In the middle column, the analogue analysis for the inter-ELM phase of a type-I ELMy H-mode is presented. Both diffusion and convection are consistent with neoclassical levels in agreement with earlier analyses (31). In the recent work, also the important net effect (32) of the ELM itself was analysed and mostly an increase of diffusive transport was inferred. In the right column the QCE regime analysis is presented, and as the small transport events could not be separated the analysis is averaging over them. In this case the diffusive transport is almost a factor of 10 larger than pure neoclassical transport and thus reduces the impurity gradients driven by neoclassical transport to much lower levels. For the typical AUG pedestal, this relates to a smaller impurity content of the confined plasma. However, for ITER the neoclassical convection is predicted outward (33) leading to hollow impurity profiles and an increase of the diffusive part might lead to less hollow impurity profiles. The underlying effect for the outward impurity convection is called temperature screening and could be qualitatively observed in AUG in specially designed discharges with high pedestal ion temperatures. Further analysis is ongoing. Another concern for a fusion reactor is the exhaust of He, as it will be constantly produced and the divertor compression and pumping efficiency is not known precisely. To that end the He pumping and compression have been investigated in the context of realistic conditions such as taking a wall retention into account (34). As a further step the whole transport chain from plasma core to pump was investigated in He seeded discharges in AUG and concomitant modelling using ITER-SOLPS including drifts (35). As important players the edge transport barrier, collisional parallel SOL-transport and the further transport

to the pumps were investigated and compared to experiment. The He compression towards the divertor from the model is about a factor of 10 lower than in experiment. However, newest findings (36) indicate that the inclusion of ELM effects in the model could resolve that open question.

### 5.3. XPR

Impurities also play a major role for the regime of the X-point radiator (XPR) (37; 38). For the access of the XPR regime a model (39) has been validated. The regime is also found in GRILLIX (40). The stable control of the regime is performed via controlling the positioning of the radiation region w.r.t. to the X-point. Too much nitrogen leads to a MARFE and thus requires disruption avoidance measures (41; 42), while already after the establishment of the XPR detachment is observed. For the regime in (43), the XPR regime becomes ELM-free when it is 7 cm above the X-point. Controlling the X-point position was also demonstrated in other machines and on AUG and JET a system identification was performed (44) in order to document the reaction of the XPR on a change in nitrogen puffing. In accordance to the observations a model was developed for the positioning of the XPR (45).

### 5.4. Negative triangularity

An alternative scenario to avoid large ELMs is the employment of negative triangularity (NT) plasma shapes, which was reported to allow for L-mode plasmas at good performance (46; 47; 48; 49; 50). In AUG, the NT shaping did not consistently avoid H-mode in the past (50; 51). In the latest campaign progress in increased NT shaping ($\delta_{upper} = -0.56$) (52) led to an avoidance of the H-mode, following also quantitatively the predictions from the infinite-n ballooning calculations (53) using BALOO, which assume that L-mode can be maintained at high heating powers, if the infinite-n ballooning boundary is blocking the path to second stability. In Fig. 11,

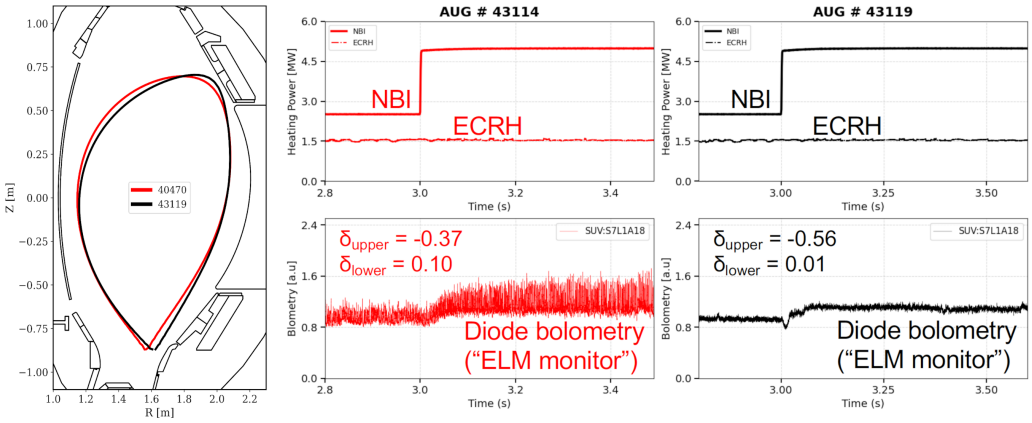


*FIG. 11. Comparison of #43114 (using the shape of #40479) with less negative triangularity to the recent discharge #43119 and an average $\delta \approx -0.275$. For the same heating power H-mode is avoided in the latter (black lines) discharges and no ELMs are visible.*

the experimental observation is summarized. Further investigations of NT plasmas did not allow access to high confinement at elevated heating powers including NBI unless nitrogen seeding was applied (52). However, the exact mechanism of this improvement remains unclear.

## 6. TRANSPORT AND STABILITY

A reevaluation of the confinement scaling with size (54) towards ITER using the IMEP (55) model revealed that the newer confinement scaling ITPA20-IL (56), which takes triangularity into account and includes also new data from JET-ILW, underestimates the model based predictions and the older prediction IPB98(y,2) (57) is in better agreement. The new model-based predictions suggest a fusion yield of $Q = 12$ for the ITER baseline scenario in ITER. The underlying confinement behaviour with higher density is consistent with the pedestal analysis in (58). Another additional result - possibly related to the observations in JET-ILW - stems from a pedestal stability analysis including non-ideal effects such as resistivity and gyroviscosity (59). It is unclear how this latter effect is captured by the scalings, or whether this effect is biasing the scalings in an unwanted direction. In various phases of a plasma discharge the radiation/transport stability of the discharge is closely interconnected with the transport processes in the core of the plasma. One important aspect for this is the avoidance of W accumulation in the core of the plasma. This phenomenon is well investigated at AUG and for an extrapolation to future fusion

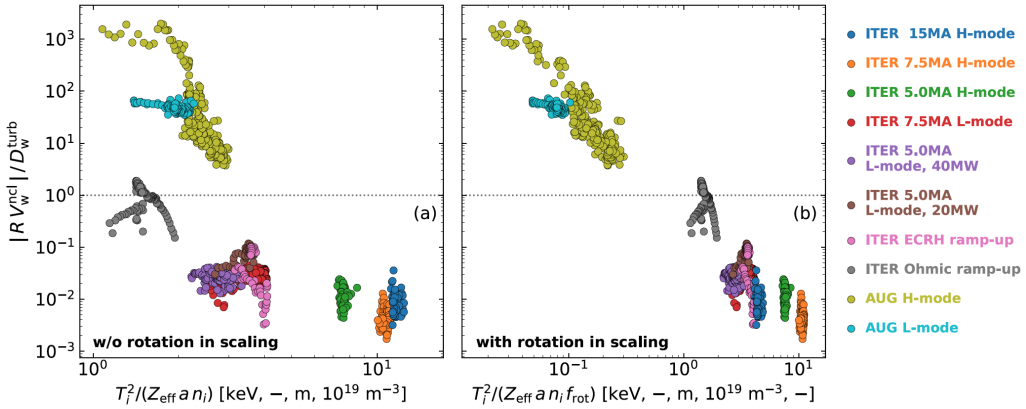


*FIG. 12. Magnitude of neoclassical drift normalized to the turbulent diffusion, adapted from (60). (a) The ratio is plotted versus a scaling formula not considering plasma rotation. (b) The ratio is plotted versus the full scaling formula including rotation.*

devices it is crucial to understand the magnitude of the neoclassical transport coefficients, which are causing the accumulation w.r.t. to the turbulent transport which typically relaxes steep impurity coefficients. This investigation uses FACIT (61) in combination with TGLF. The modelling chain was first benchmarked to describe the core impurity transport in AUG (62; 63). Further, the different kinds of ITER plasmas were in vestigated and a scaling was developed to describe the importance of the neoclassical drift relative to the turbulent diffusion coefficient. In Fig.12, the relative size of the neoclassical and turbulent transport is depicted. For the ITER cases the neoclassical drift is generally less important than for the AUG cases, which also include cases with strong central electron heating. All data follows considerably well the scaling formula developed in (60) only if the plasma rotation is taken into account, as can be inferred via the comparison of Fig.12(a) and Fig.12(b). In order to better predict the rotation intrinsic plasma rotation needs to be better understood, as especially for ITER external torque sources are small. Investigations in this respect have been conducted. First the disentanglement of external and internal torque sources was performed via beam modulation experiments (64) in D and H plasmas (65). Second the results were compared to gyrokinetic predictions (66) on intrinsic core torque and good agreement was found, which was the basis for developing a reduced model for fast predictions.

The ramp-down phase from the flattop of the ITER baseline scenario has been investigated via RAPTOR (67; 68) and similar findings could be reproduced by modelling the ITER baseline ramp-downs using the flight simulator FENIX (69; 70). In Fig.13(a) the trajectories of one discharge are presented along with the modelled curves from FENIX. The main focus of this work was to find strategies to keep the internal inductance (here $\ell_i(3)$) as small as possible as this relates to controllability of the plasma position. Major effects on $\ell_i(3)$ were found to be caused by the HL-transition (vertical, dashed line) and the normalized current ramp rate, here represented as $\Delta I_p/I_p$. The need for normalization becomes visible in Fig.13 were only after normalization an almost linear correlation to the change in $\ell_i(3)$, i.e. $\Delta\ell_i(3)$, becomes apparent. FENIX is constantly improved and reduced models (71) are developed and validated for this purpose.

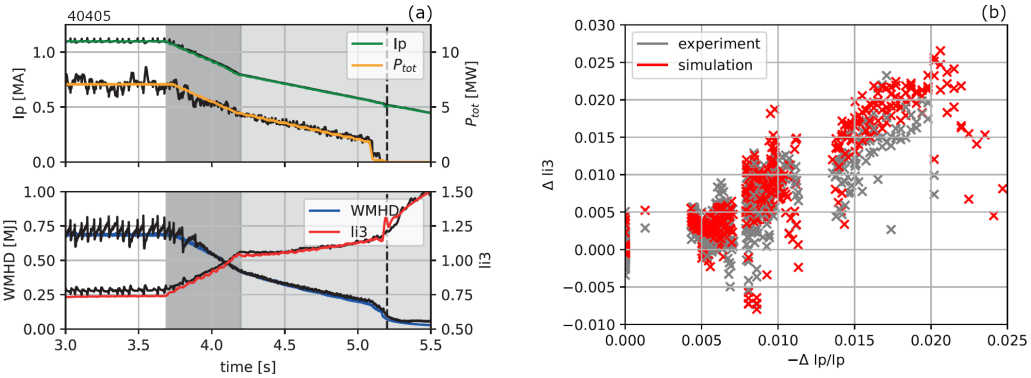


*FIG. 13. (a) Measured (black) and modelled (coloured) time traces for a ramp-down from an ITER baseline scenario in AUG. Phases with a different current ramp rate are highlighted with the shaded areas. (b) The increase in $\ell_i(3)$ is a function of the normalized current ramp rate for both experiment and FENIX simulation.*

## 7. SPI FOR DISRUPTION MITIGATION

At AUG a shattered pellet injection (SPI) system (72) has been characterized and installed in order to identify the best strategies for disruption mitigation and runaway suppression in ITER. One of the recent results is depicted in Fig.14. For a variety of Ne amounts in the pellet the current decays are compared (73). For small amounts of Ne the current decay is slow and in fact was in experiment so slow, that vertical displacement events did show up before the actual decay to zero. With increasing amounts of Ne the energy was more rapidly removed from the plasma via better assimilation and radiation and the current could dissipate its energy faster suggesting a safer end of the discharge in terms of forces. However, the faster decay implies larger loop voltages and thus a higher probability to obtain runaway electrons. Thus, the Ne fraction allows for tailoring the current decay minimizing forces and runaway electrons.

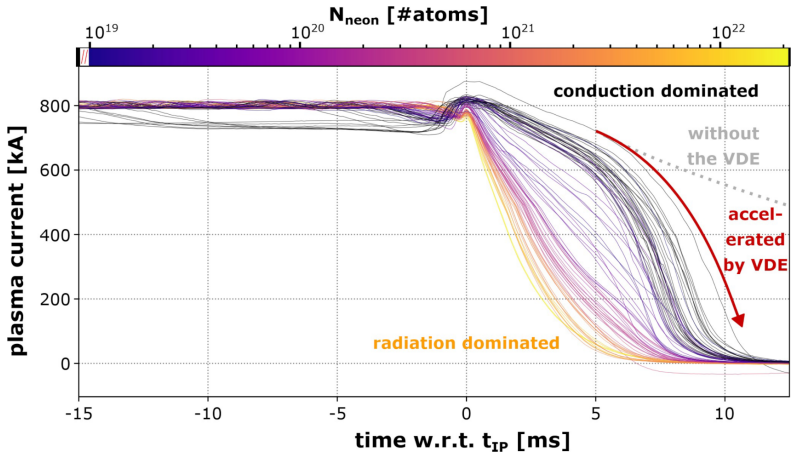


*FIG. 14. Current trajectories for many disruptions, which were triggered via SPI with various amounts of Ne in the pellets. The current quench systematically changes with the Ne amount.*

## 8. SUMMARY AND CONCLUSIONS

After a 26-month vent AUG went back in operation featuring a new upper divertor with a dedicated cryo-pump and in-vessel coils for obtaining alternative divertor configurations (ADC). All envisaged configurations could be created and investigated. A large diagnostic suite led to a collection of a large data set, which is in the process of being analysed and interpreted. In ADCs plasmas large scans of heating (up to 20 MW), fuelling and seeding were performed and the onset of detachment in the outer divertor could be observed, while the inner divertor was always detached. The neutral compression is consistent with an open divertor and can be improved via the planned installation of baffels. This upgrade is subsequent to the identification of the most promising ADC, which is best judged with the full set of diagnostics only available with an open divertor. The restart provided the opportunity to study the challenges of an unboronized startup and proved that the W erosion also during the limiter phase is unimportant in cases when low-Z impurities lead to large radiative losses. However, these losses also imply large loop voltages and consequently yield the danger of creating large runaway populations. The subsequent boronizations were studied in terms of breaking the symmetry on purpose by only using a subset of the glow anodes during the glow discharge used for boronization. The resulting boron layers however, were much more symmetric than expected, hinting towards a more free choice for the locations of the glow anodes in ITER. Future fusion devices must avoid the detrimental type-I ELMs. AUG explored several strategies with that aim. The QCE/EDA regimes exhibit small-ELM or no ELMs and show promising power exhaust while maintaining confinement. Pedestal stability analyses linked QCE to the local infinite-n ballooning limit near the separatrix, with plasma shaping (elongation, triangularity) enabling access. An alternative approach for avoiding ELMs is the XPR featuring controllable detachment and ELM suppression for the correct XPR position, which was demonstrated to be consistently controllable. Another route to avoiding ELMs is utilizing negative triangularity shapes as was demonstrated in DIII-D and TCV. The underlying idea to destabilize infinite-n ballooning modes via more negative triangularity shaping succeeded now also at AUG and demonstrated H-mode avoidance at high heating powers. Impurity transport at the plasma edge was investigated using Bayesian inference on density measurements of $Ne^{8+}$ to $Ne^{10+}$. As a result the diffusive and convective Ne transport was quantified, showing turbulent contributions beyond neoclassical predictions in L-mode and QCE phases, which mitigates impurity accumulation. Also advances on the analysis of He exhaust have been achieved, elaborating several specialities of He, but also demonstrating the importance

of taking the effect of ELMs into account. Updated confinement scalings using the integrated modelling approach IMEP suggests ITER may achieve Q=12, clearly higher than recent ITPA20-IL predictions. Recent pedestal stability analyses including resistive and gyroviscous effects reproduce density-dependent reductions in stability. The integrated modelling of core impurity transport highlighted the lower importance of neoclassical vs. turbulent transport in ITER, with plasma rotation critically influencing predictions. The simulations (here flight-simulator FENIX) of ramp-down from the ITER baseline flattop identified normalized current ramp rate and H–L transition as key factors in controlling internal inductance. AUG investigated pellets from the shattered pellet injector to study safe discharge termination. Results showed that higher neon content in the pellets accelerated current decay, reducing mechanical forces but increasing loop voltages and risks of creating runaways. These findings inform ITER strategies for disruption control. In summary, the AUG upgrades and experiments provide essential benchmarks for ITER, advancing knowledge in start-up conditioning, tungsten erosion, divertor optimization, ELM control strategies, impurity transport, confinement scaling, and disruption mitigation. The insights significantly enhance predictive capability towards ITER's operation, especially after moving to a full-W wall.

## ACKNOWLEDGEMENTS

This work has been carried out within the framework of the EUROfusion Consortium, funded by the European Union via the Euratom Research and Training Programme (Grant Agreement No 101052200 — EUROfusion). Views and opinions expressed are however those of the author(s) only and do not necessarily reflect those of the European Union or the European Commission. Neither the European Union nor the European Commission can be held responsible for them.

## REFERENCES

[1] I. Zammuto, A. Herrmann, et al., Fusion Engineering and Design **215**, 115028 (2025).
[2] A. Herrmann, M. Teschke, et al., Fusion Engineering and Design **146**, 920–923 (2019), SI:SOFT-30.
[3] M. Teschke, A. Herrmann, et al., Fusion Engineering and Design **146**, 1181–1185 (2019), SI:SOFT-30.
[4] G. Schall, N. Berger, et al., Fusion Engineering and Design **166**, 112316 (2021).
[5] T. Lunt, H. Zohm, et al., Nuclear Materials and Energy **12**, 1037–1042 (2017), Proceedings of the 22nd International Conference on Plasma Surface Interactions 2016, 22nd PSI.
[6] A. Kallenbach, R. Dux, et al., Plasma Physics and Controlled Fusion **67**(8), 085005 (2025).
[7] V. Rohde, M. Balden, et al., Nuclear Materials and Energy **43**, 101923 (2025).
[8] A. Kallenbach, R. Dux, et al., Nuclear Fusion **49**(4), 045007 (2009).
[9] R. Neu, V. Bobkov, et al., Physica Scripta **2009**(T138), 014038 (2009).
[10] V. Rohde, K. Kieger, et al., Investigations on boronisation in the full-tungsten ASDEX Upgrade, 2025, PFMC-20, Ljubljana, Slovenia.
[11] J. Hobirk, R. Pitts, et al., Tungsten limiter start-up experiments in differentboronization states in support of ITER, 2025, this conference, IAEA-CN-392/EX-C-3308.
[12] M. Mayer, S. An, et al., Surface Loss Probabilities of Boron-hydride Radicals in W7-X and ASDEX Upgrade, 2025, PFMC-20, Ljubljana, Slovenia.
[13] T. Wauters, G. Hagelaar, et al., Nuclear Materials and Energy **42**, 101891 (2025).
[14] A. Loarte, R. A. Pitts, et al., Plasma Physics and Controlled Fusion **67**(6), 065023 (2025).
[15] K. Schmid and T. Wauters, Nuclear Materials and Energy **41**, 101789 (2024).
[16] R. Pitts, A. Loarte, et al., Nuclear Materials and Energy **42**, 101854 (2025).
[17] T. Lunt, F. Albrecht, et al., First campaign with Alternative Divertor Configurations in ASDEX Upgrade, 2025, this conference, IAEA-CN-392/postdeadline.
[18] M. Faitsch, M. Dunne, et al., Nuclear Materials and Energy **42**, 101904 (2025).
[19] L. Gil, T. Pütterich, et al., Nuclear Fusion **65**(4), 046002 (2025).
[20] J. Kalis, G. Birkenmeier, et al., Nuclear Fusion **64**(1), 016038 (2023).
[21] M. Faitsch, T. Eich, et al., Nuclear Materials and Energy **26**, 100890 (2021).
[22] M. Faitsch, T. Eich, et al., Nuclear Fusion **63**(7), 076013 (2023).
[23] A. Redl, T. Eich, et al., Nuclear Fusion **64**(8), 086064 (2024).
[24] M. Faitsch, M. Dunne, et al., Nuclear Fusion **65**(2), 024003 (2025).
[25] L. Radovanovic, M. Dunne, et al., Nuclear Fusion **62**(8), 086004 (2022).
[26] L. Radovanovic, E. Wolfrum, et al., Nuclear Fusion **65**(5), 056039 (2025).
[27] M. Dunne, M. Faitsch, et al., Nuclear Fusion **64**(12), 124003 (2024).
[28] W. Zholobenko, K. Eder, et al., Validated, global edge-SOL turbulence simulations in various ELM-free regimes, 2025, this conference, IAEA-CN-392/3241.
[29] W. Zholobenko, K. Zhang, et al., Nuclear Fusion **64**(10), 106066 (2024).

[30] T. Gleiter, R. Dux, et al., Nuclear Fusion **65**(5), 056010 (2025).
[31] T. Pütterich, R. Dux, et al., Journal of Nuclear Materials **415**(1, Supplement), S334–S339 (2011), Proceedings of the 19th International Conference on Plasma-Surface Interactions in Controlled Fusion.
[32] R. Dux, A. Loarte, et al., Nuclear Materials and Energy **12**, 28–35 (2017), Proceedings of the 22nd International Conference on Plasma Surface Interactions 2016, 22nd PSI.
[33] R. Dux, A. Loarte, et al., Plasma Physics and Controlled Fusion **56**(12), 124003 (2014).
[34] A. Zito, M. Wischmeier, et al., Nuclear Fusion **63**(9), 096027 (2023).
[35] A. Zito, O. Pan, et al., Nuclear Fusion **65**(4), 046022 (2025).
[36] A. Zito, M. Cavedon, et al., Numerical assessment of the impact of ELM flushingon impurity exhaust in ASDEX Upgrade H-modes, 2025, 20th International Workshop on Plasma EdgeTheory in Fusion Devices (PET-20).
[37] T. Lunt, M. Bernert, et al., Phys. Rev. Lett. **130**, 145102 (2023).
[38] M. Bernert, T. Bosman, et al., Nuclear Materials and Energy **43**, 101916 (2025).
[39] U. Stroth, M. Bernert, et al., Nuclear Fusion **62**(7), 076008 (2022).
[40] K. Eder, A. Stegmeir, et al., Plasma Physics and Controlled Fusion **67**(6), 065034 (2025).
[41] B. Sieglin, M. Maraschek, et al., Plasma Physics and Controlled Fusion **66**(2), 025004 (2023).
[42] B. Sieglin, M. Maraschek, et al., Fusion Engineering and Design **215**, 114961 (2025).
[43] M. Bernert, F. Janky, et al., Nuclear Fusion **61**(2), 024001 (2020).
[44] T. Bosman, M. Bernert, et al., Nuclear Fusion **65**(1), 016057 (2024).
[45] U. Stroth, M. Bernert, et al., Plasma Physics and Controlled Fusion **67**(3), 035001 (2025).
[46] A. Pochelon, T. Goodman, et al., Nuclear Fusion **39**(11Y), 1807 (1999).
[47] Y. Camenen, A. Pochelon, et al., Nuclear Fusion **47**(7), 510 (2007).
[48] M. E. Austin, A. Marinoni, et al., Phys. Rev. Lett. **122**, 115001 (2019).
[49] A. Marinoni, O. Sauter, et al., Reviews of Modern Plasma Physics **5**(1), 6 (2021).
[50] T. Happel, T. Pütterich, et al., Nuclear Fusion **63**(1), 016002 (2022).
[51] B. Vanovac, M. Dunne, et al., Plasma Physics and Controlled Fusion **66**(11), 115005 (2024).
[52] B. Vanovac, J. Hobirk, et al., Overview of negative triangularity experiments with strong shaping in ASDEX Upgrade, 2025, 67th Annual Meeting of the APS Division of Plasma Physics.
[53] A. Nelson, C. Paz-Soldan, et al., Nuclear Fusion **62**(9), 096020 (2022).
[54] T. Luda, C. Angioni, et al., Nuclear Fusion **65**(7), 072001 (2025).
[55] T. Luda, C. Angioni, et al., Nuclear Fusion **60**(3), 036023 (2020).
[56] G. Verdoolaege, S. Kaye, et al., Nuclear Fusion **61**(7), 076006 (2021).
[57] ITER Physics Expert Group on Confinement and Transport and ITER Physics Expert Group on Confinement Modelling and Database and ITER Physics Basis Editors, Nuclear Fusion **39**(12), 2175 (1999).
[58] L. Frassinetti, D. King, et al., Peeling limited pedestals in JET-ILW, MAST-U and TCV: Effect of density and isotope mass in deuterium and tritium-rich plasma on pedestal structure and stability and validation of pedestal predictions for ITER, 2025, this conference, IAEA-CN-392/2845.
[59] F. Stefanelli, M. Dunne, et al., Nuclear Fusion **65**(8), 086025 (2025).
[60] D. Fajardo, C. Angioni, et al., Plasma Physics and Controlled Fusion **67**(1), 015020 (2024).
[61] D. Fajardo, C. Angioni, et al., Plasma Physics and Controlled Fusion **65**(3), 035021 (2023).
[62] D. Fajardo, C. Angioni, et al., Nuclear Fusion **64**(10), 104001 (2024).
[63] D. Fajardo, C. Angioni, et al., Nuclear Fusion **64**(4), 046021 (2024).
[64] C. F. B. Zimmermann, R. M. McDermott, et al., Plasma Physics and Controlled Fusion **64**(5), 055020 (2022).
[65] C. Zimmermann, R. McDermott, et al., Nuclear Fusion **63**(12), 126006 (2023).
[66] C. F. B. Zimmermann, C. Angioni, et al., Physics of Plasmas **31**(4), 042306 (2024).
[67] S. Van Mulders, O. Sauter, et al., Plasma Physics and Controlled Fusion **66**(2), 025006 (2023).
[68] S. Van Mulders, O. Sauter, et al., Plasma Physics and Controlled Fusion **66**(2), 025007 (2023).
[69] E. Fable, F. Janky, et al., Plasma Physics and Controlled Fusion **64**(4), 044002 (2022).
[70] P. David, E. Fable, et al., Open Plasma Science **Volume 1** (2025).
[71] F. Solfronk, E. Fable, et al., Nuclear Fusion **65**(8), 086020 (2025).
[72] M. Dibon, P. de Marne, et al., Review of Scientific Instruments **94**(4), 043504 (2023).
[73] P. Heinrich, G. Papp, et al., Nuclear Fusion **65**(5), 056036 (2025).